Supplementary Information

Continuous and sustainable electrosynthesis of free hydroxylamine enabled by a self-regenerative catalyst system

*Rui Zhou[1,2], Bairan He[1,2], Mohsen Tamtaji[3], Zhengxiao Guo[1], GuanHua Chen[1,3], Edmund C. M. Tse[1,2]**

[1]Department of Chemistry, The University of Hong Kong, Hong Kong SAR, China.

[2]HKU-CAS Joint Laboratory on New Materials, The University of Hong Kong, Hong Kong SAR, China.

[3]Hong Kong Quantum AI Lab Limited, Pak Shek Kok, Hong Kong SAR, China.

Email: ecmtse@hku.hk

Supplementary methods

Material characterizations

X-ray diffraction (XRD) patterns were collected from the Rigaku MiniFlex 600 benchtop X-ray diffraction instrument. Scanning electron microscopy (SEM) images were examined using a LEO 1530 scanning electron microscope. Transmission electron microscopy (TEM) and scanning transmission electron microscopy (STEM) were characterized by Thermo Scientific Talos F200X STEM at 200 kV.

Operando Raman measurements

The operando Raman measurements were conducted in a customized single cell with a glassy carbon as the working electrode, Ag/AgCl as the reference electrode, and a platinum wire as the counter electrode. Spectral data were collected using the Horiba LabRAM Odyssey Nano spectrometer with a laser wavelength of 532 nm. A solution of 0.5 M HNO_3 + 20 ppm Bi^{3+} was used as the electrolyte. During the measurements, the potential was first set at -1.4 V vs. RHE for 30 min and then switched to open-circuit state. Raman signals were collected to probe the bismuth species on electrode surface with an exposure time of 20 s (averaged for three scans to enhance signal-to-noise ratio) and a laser power of 25%.

COMSOL Multiphysics Simulations

Finite element method (FEM) simulations were performed using COMSOL Multiphysics v6.3. Guided by TEM observations of post-catalysts from commercial Bi_2O_3 and Bi^{3+}-regenerative system, spherically tipped conical nanotip structures with apex diameter of 500 and 30 nm were conducted using a 2D axisymmetric configuration. The Electric Currents (ec) module was employed to simulate the local electric field distribution under an applied voltage of -1.4 V, governed by the formula: $E = -\nabla V$. Extremely fine triangular meshes were utilized throughout the computational domain to ensure numerical convergence. The electric conductivities of the metallic Bi electrode and the bulk electrolyte were defined as 7.7×10^5 and 5 S m^{-1}, respectively.

Density functional theory calculations

The spin-polarized density functional theory (DFT) was applied in the Vienna ab initio simulation package (VASP 6.1.0) with the Perdew-Burke-Emzerhof (PBE) functional and a plane-wave cutoff energy of 500 eV[1]. A 3×3 supercell of Bi (012) (13.614Å×14.604Å) was constructed[2]. To avoid interaction between the two layers, a vacuum layer was set to be 30 Å in the slab model. The Brillouin zone was sampled using a 3×3×1 k-point grid for structural relaxation and a 5×5×1 grid for self-consistent calculations, both within the Γ-point scheme. The DFT-D3 method was used to consider van der Waals dispersion interactions, and VASPsol was used to account for implicit solvation. For structural relaxation, the convergence criteria for the electronic structure energy and force on each atom were set to be 10^{-5} eV and 0.025 eV/Å, respectively. For self-consistent calculations, the convergence criteria for the electronic structure energy were set to be 10^{-6} eV. The change of Gibbs free energy ($\Delta G_{*\text{int.}}$) of intermediates (int.) was calculated as[3]:

$$\Delta G_{*\text{int.}} = \Delta E_{*\text{int.}} + \Delta ZPE - T\Delta S \quad \text{(S1)}$$

where ΔZPE is the zero-point energy change, ΔS is the entropy change, and T is the reaction temperature (=300 K). $\Delta E_{*\text{int.}}$ is the adsorption energy of intermediates (int.).

To circumvent the direct calculation of the energy of charged NO_3^-, we adopted gaseous HNO_3 as a reference. The adsorption energy of NO_3^- (ΔG_{*NO_3}) was determined as follows[4]:

$$\Delta G_{*NO_3} = G_{*NO_3} - G_{*} - G_{HNO_3(g)} + \frac{1}{2}G_{H_2(g)} + \Delta G_{\text{correct}} \quad \text{(S2)}$$

In this equation, G_{*NO_3}, G_{*}, $G_{HNO_3(g)}$, and $G_{H_2(g)}$ denote the intrinsic Gibbs free energies of adsorbed NO_3^-, bare Bi (012), gas-phase HNO_3, and gas-phase H_2, respectively. Additionally, $\Delta G_{\text{correct}}$ represents the correction for NO_3^- adsorption energy, set to 0.392 eV.

The total reaction of NO_3RR can be expressed as $NO_3^- + 7H^+ + 6e^- \rightarrow NH_2OH + 2H_2O$. Below shows the detailed formula of all elementary processes observed during the search for minimum energy reaction pathways.

$$* + NO_3^- \rightarrow *NO_3 + e^- \quad \text{(S3)}$$

$*NO_3 + (H^+ + e^-) \rightarrow *NO_3H$ (S4)

$*NO_3H + (H^+ + e^-) \rightarrow *NO_2 + H_2O$ (S5)

$*NO_2 + (H^+ + e^-) \rightarrow *NO_2H$ (or $*NHO_2$) (S6)

$*NO_2 \rightarrow * + NO_2$ (S7)

$*NO_2H + (H^+ + e^-) \rightarrow *NO + H_2O$ (S7)

$*NO_2H$ (or $*NHO_2$) $\rightarrow$ * + NO_2H (or * + NHO_2)

$*NO + (H^+ + e^-) \rightarrow *NHO$ (or *NOH) (S8)

$*NO \rightarrow * + NO$

$*NHO + (H^+ + e^-) \rightarrow *NH_2O$ (or *NHOH) (S9)

$*NOH \rightarrow * + NOH$

$*NH_2O + (H^+ + e^-) \rightarrow *NH_2OH$ (S10)

$*NHOH \rightarrow * + NHOH$

$*NH_2OH \rightarrow * + NH_2OH$ (S11)

Supplementary figures

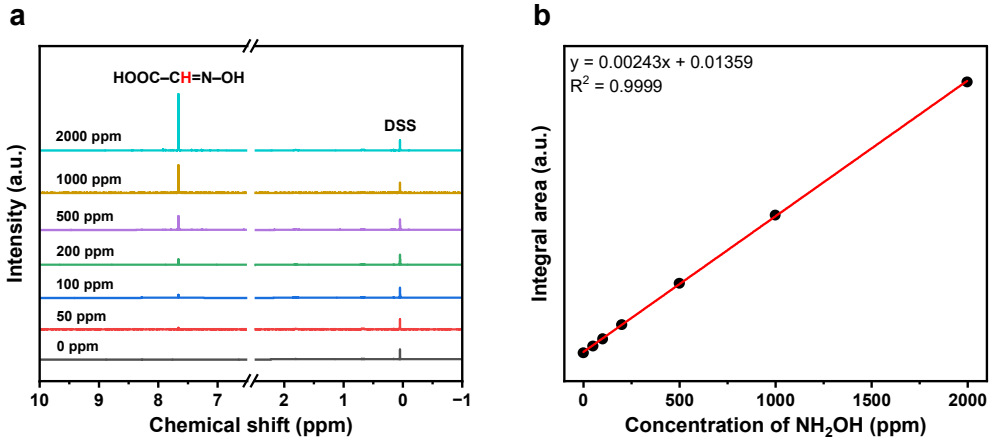

Supplementary Fig. 1 | a, Quantification of glyoxylic acid oxime with different concentrations of NH_2OH by ^1H NMR method. **b,** Calibration curve of NH_2OH.

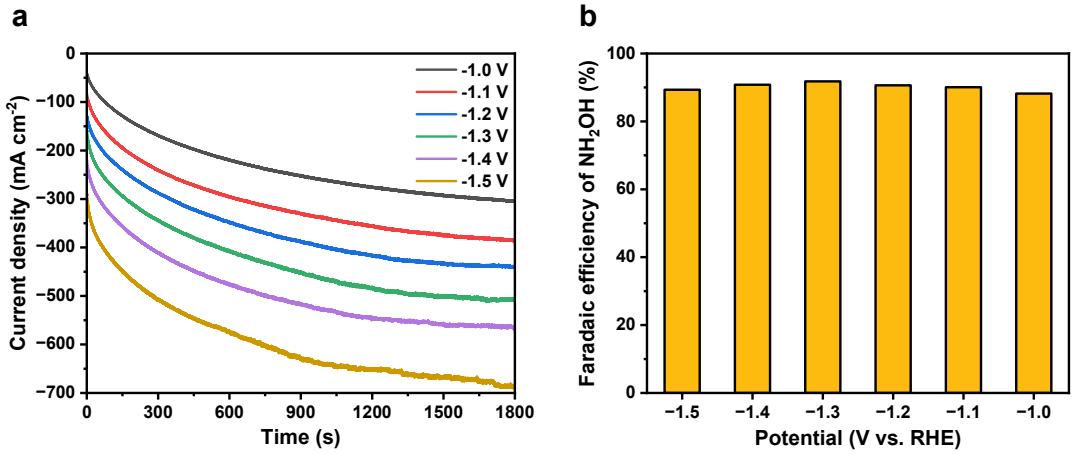

Supplementary Fig. 2 | a, Chronoamperometry measurements between -1.0 and -1.5 V vs. RHE in the electrolyte of 0.5 M HNO_3 containing 20 ppm Bi^{3+}. **b,** Faradaic efficiency of NH_2OH product at the applied potentials.

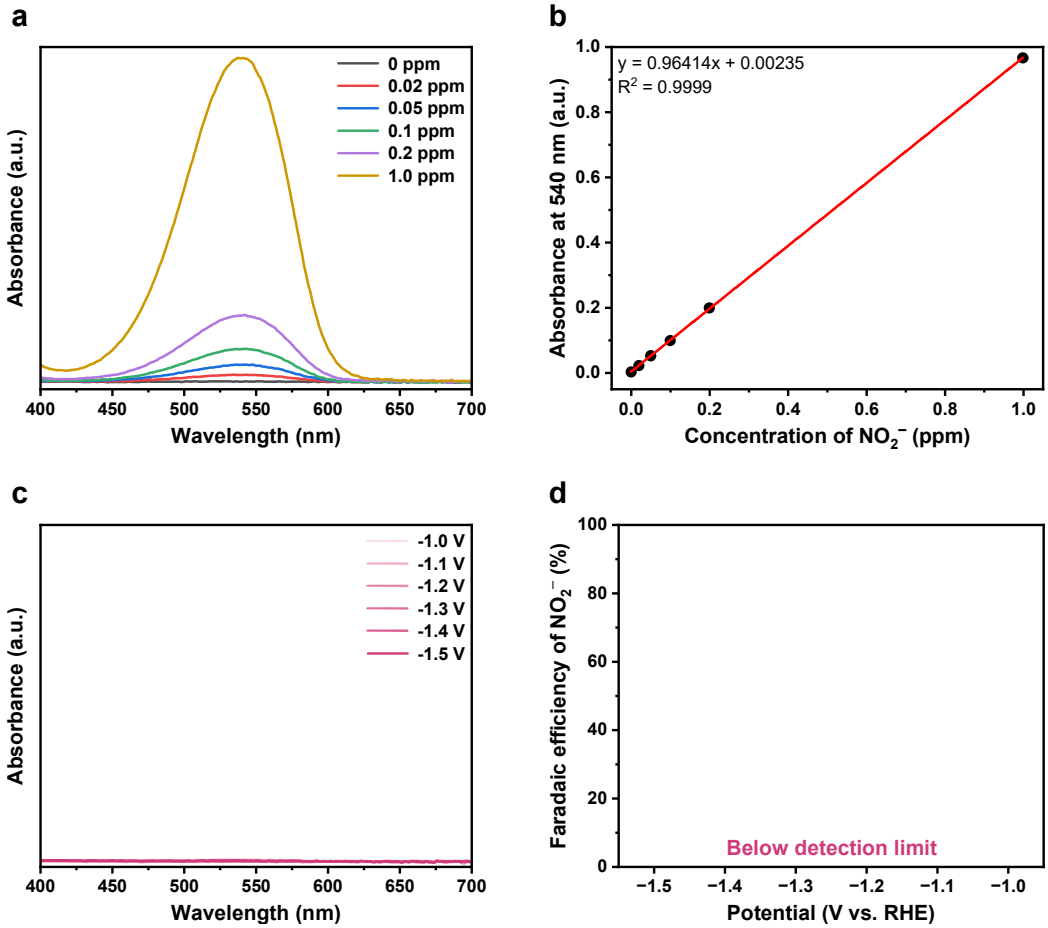

Supplementary Fig. 3 | a, Quantification of NO_2^- by colorimetric method. **b,** Calibration curve of NO_2^-. **c,** NO_2^- absorbance of post-electrolyte samples after the applied potentials. **d,** Faradaic efficiency of NO_2^- product at the applied potentials.

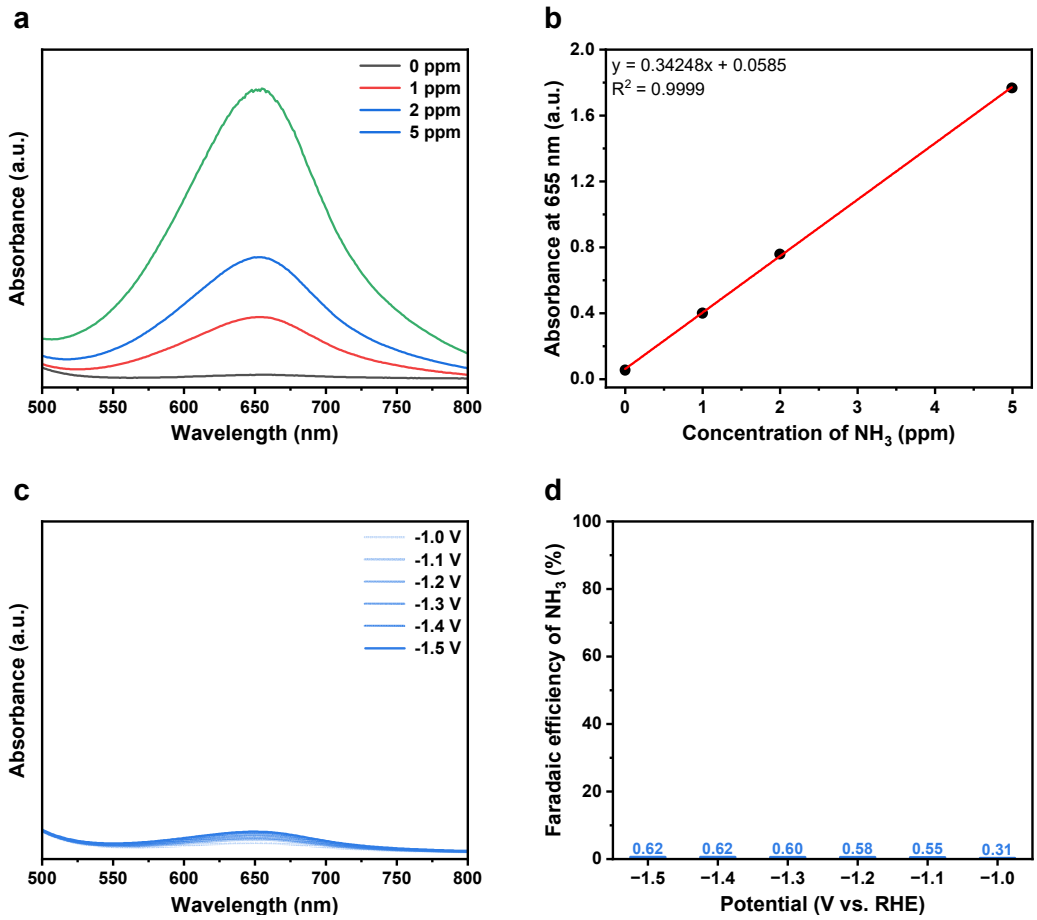

Supplementary Fig. 4 | a, Quantification of NH_3 by colorimetric method. **b,** Calibration curve of NH_3. **c,** NH_3 absorbance of post-electrolyte samples after the applied potentials. **d,** Faradaic efficiency of NH_3 product at the applied potentials.

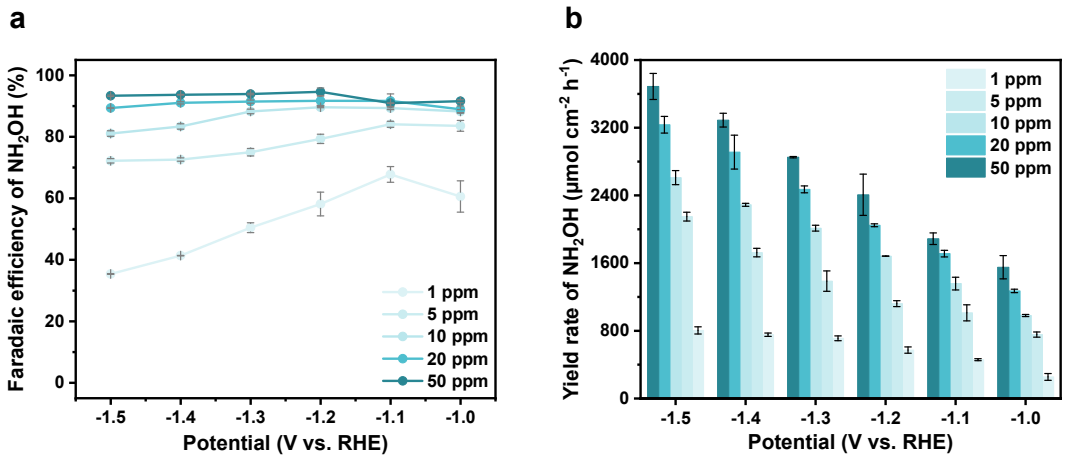

Supplementary Fig. 5 | Faradaic efficiency **(a)** and yield rate **(b)** of NH_2OH under different potentials in 0.5 M HNO_3 electrolytes containing varying concentrations of Bi^{3+}.

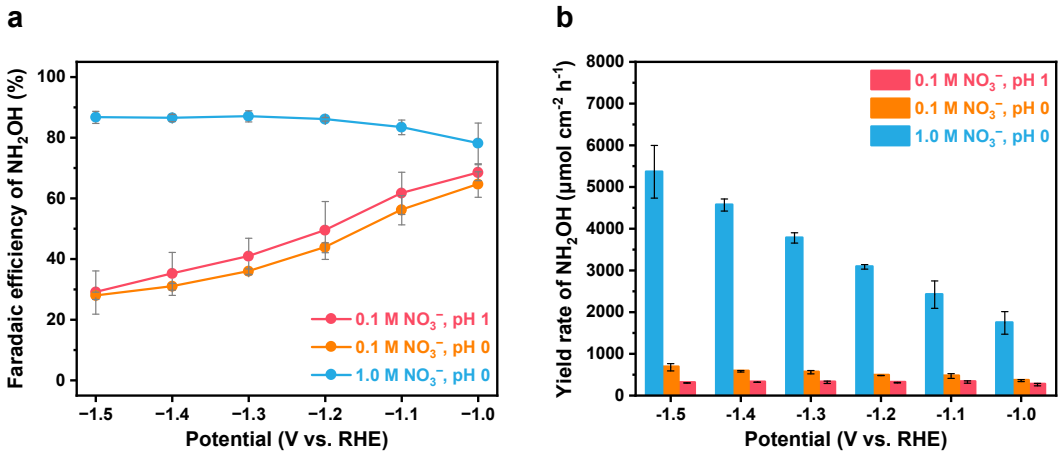

Supplementary Fig. 6 | Faradaic efficiency **(a)** and yield rate **(b)** of NH_2OH in acidic electrolytes containing 20 ppm Bi^{3+} across various pH and nitrate concentrations.

To study the influence of proton concentration without potential interference from alkali metal cations, control experiments were conducted under three conditions: 0.1 M HNO_3 (pH 1), 0.1 M HNO_3 adjusted to pH 0 with H_2SO_4, and 1 M HNO_3 (pH 0). As shown in Supplementary Fig. 6, nearly identical FE and yield rate of NH_2OH are observed for 0.1 M NO_3^- at both pH 0 and 1 across all applied potentials. This observation suggests that proton concentration has a negligible impact on the electrosynthesis of NH_2OH within this pH range. In contrast, a substantial disparity in NH_2OH production is observed when the nitrate concentration is increased at a constant pH. These findings validate our conclusion that nitrate concentration rather than pH (within 0-1 range) is the predominant factor governing the reaction kinetics of electrochemical NO_3^--to-NH_2OH conversion in our system.

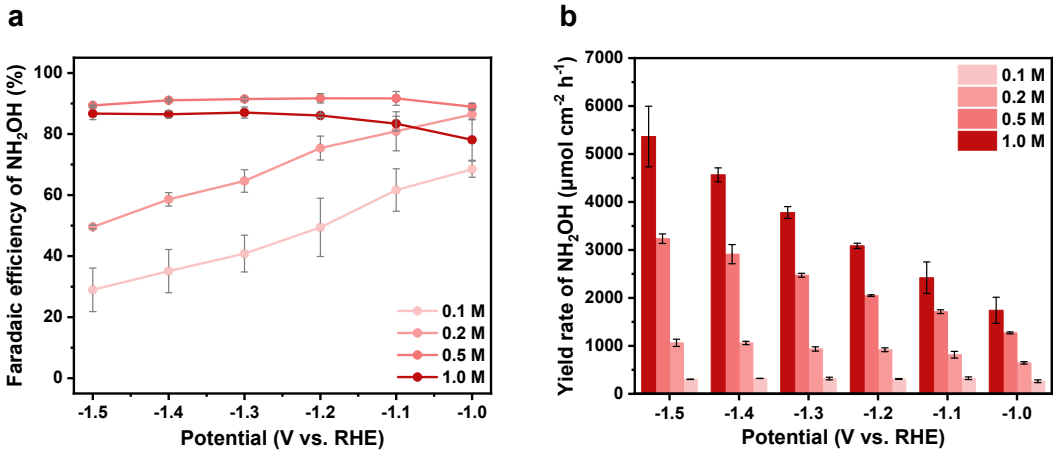

Supplementary Fig. 7 | Faradaic efficiency **(a)** and yield rate **(b)** of NH_2OH under different potentials in x M HNO_3 (x = 0.1, 0.2, 0.5, and 1) electrolytes containing 20 ppm Bi^{3+}.

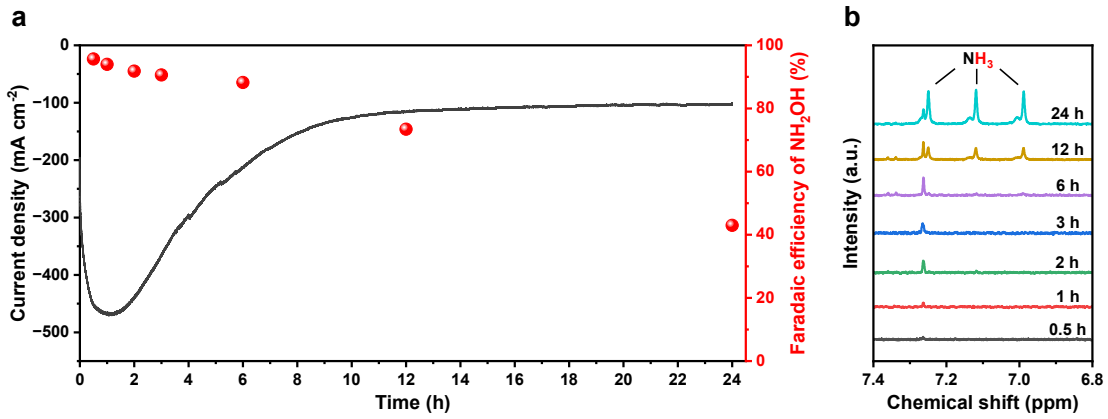

Supplementary Fig. 8 | a, 24-h chronoamperometry measurement and relevant NH_2OH FEs at -1.4 V vs. RHE in 30 mL of 0.5 M HNO_3 containing 20 ppm Bi^{3+}. **b,** Detection of NH_3 product using ^1H NMR during 24-h electrolysis.

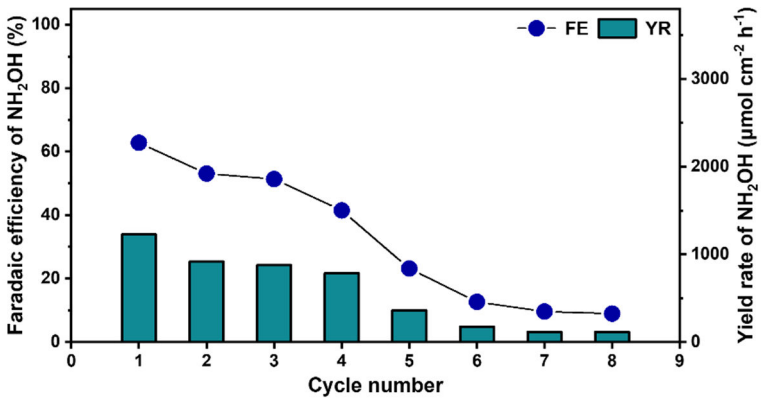

Supplementary Fig. 9 | 8 consecutive cycles for commercial Bi_2O_3 at -1.4 V vs. RHE in 0.5 M HNO_3.

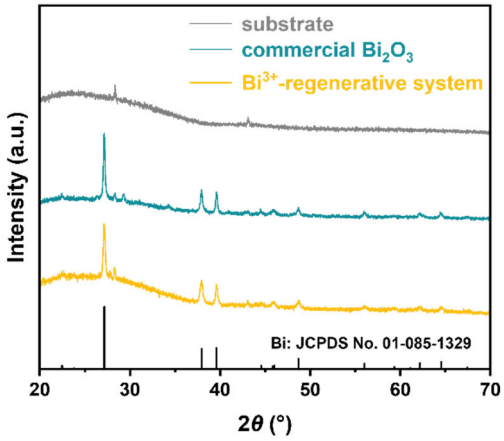

Supplementary Fig. 10 | XRD patterns for catalysts derived from commercial Bi_2O_3 and Bi^{3+}-regenerative system after electrolysis.

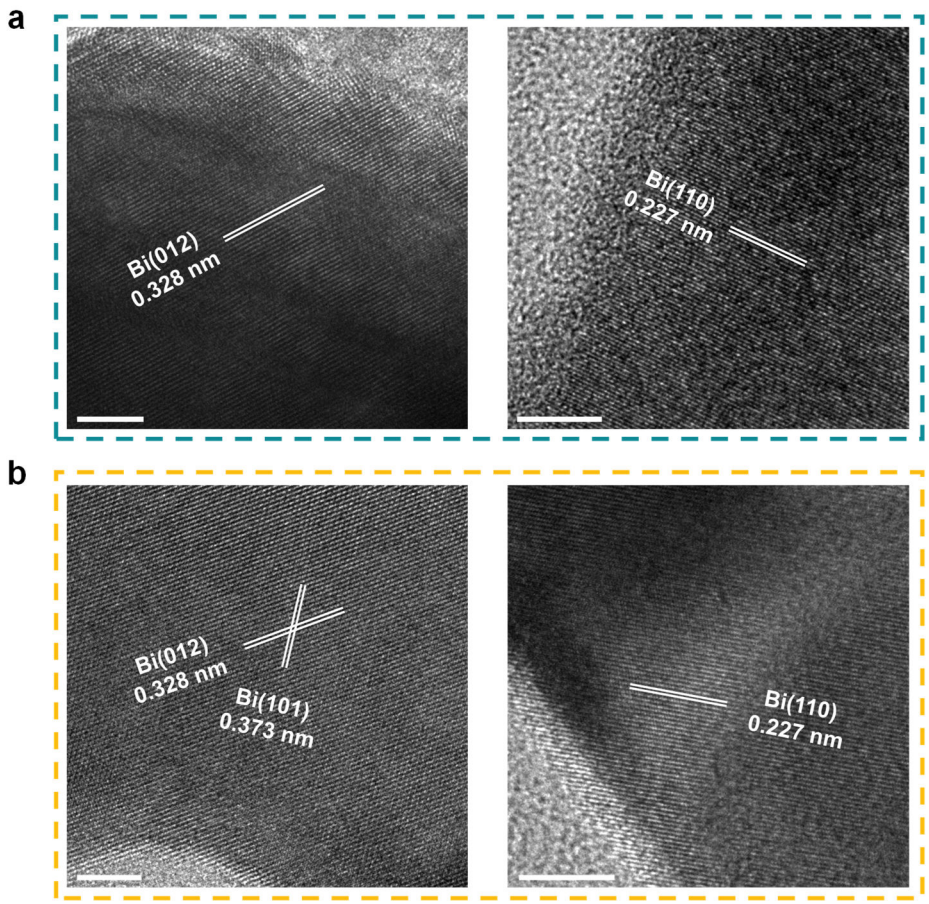

Supplementary Fig. 11 | High-resolution TEM images for the catalysts after electrolysis from **(a)** commercial Bi_2O_3 and **(b)** Bi^{3+}-regenerative system. Scale bar: 5 nm.

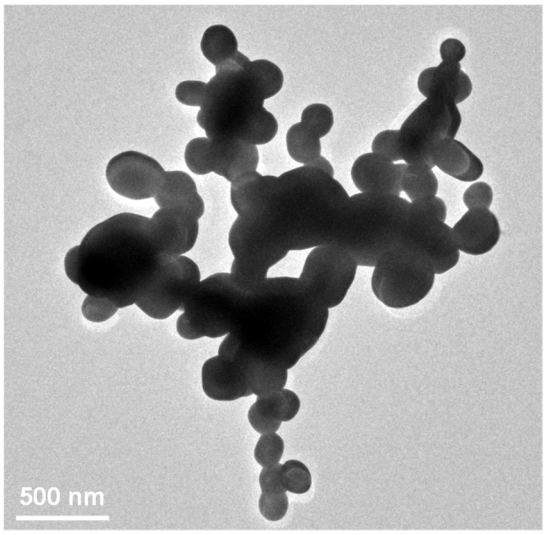

Supplementary Fig. 12 | TEM image of commercial Bi_2O_3 nanoparticles.

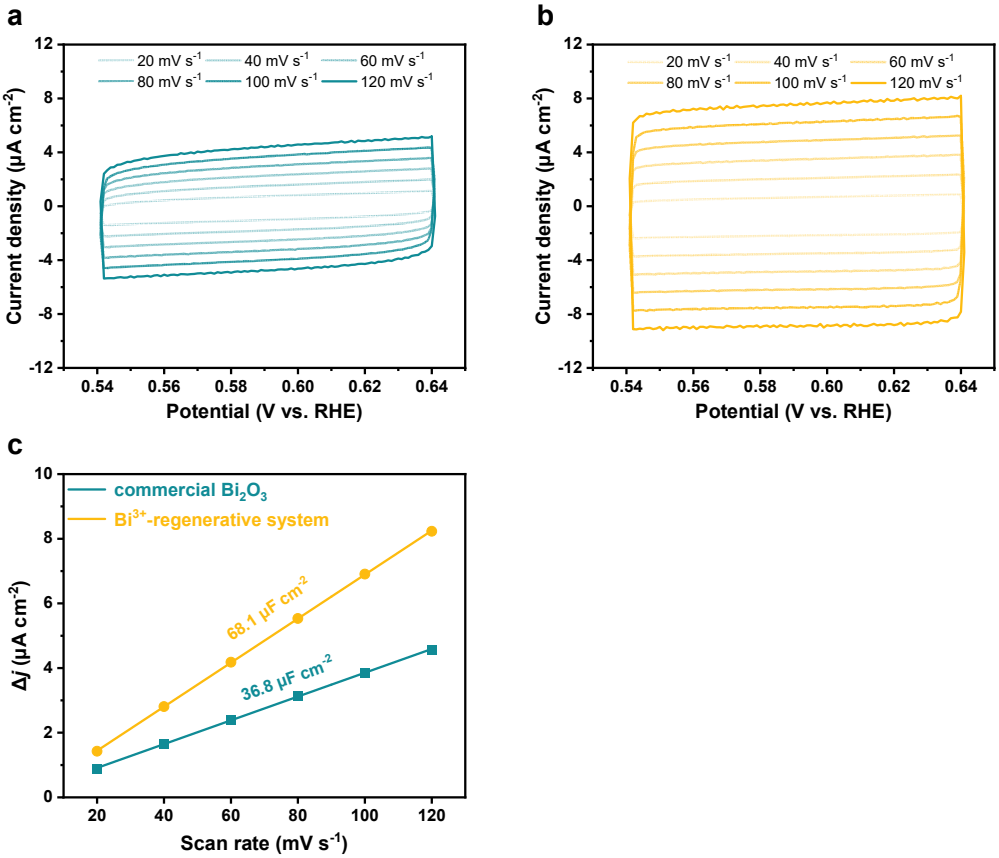

Supplementary Fig. 13 | CV curves acquired at different scanning rates for **(a)** commercial Bi_2O_3 and **(b)** Bi^{3+}-regenerative system. **c,** Calculated electrochemical double-layer capacitance of two catalysts from the differences in current densities at 0.59 V vs. RHE.

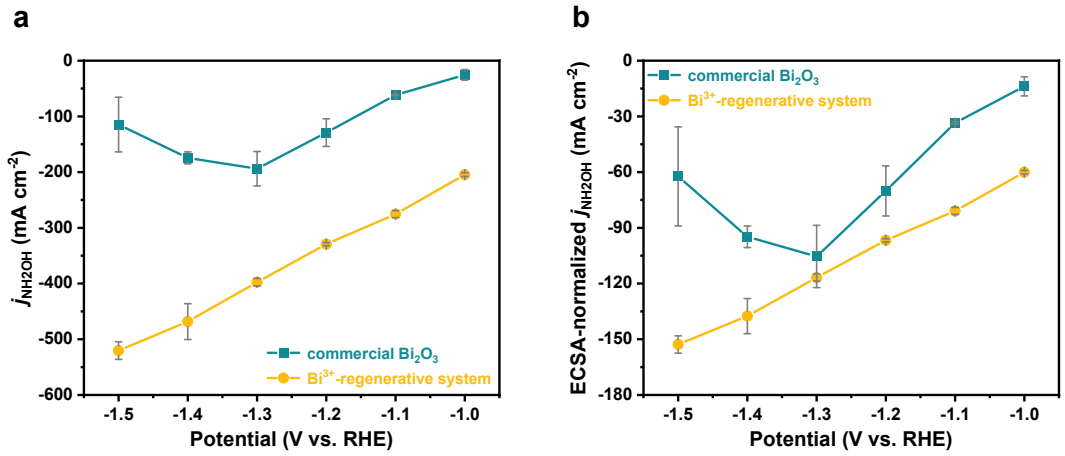

Supplementary Fig. 14 | a, Partial current densities of NH_2OH for commercial Bi_2O_3 and Bi^{3+}-regenerative system. **b,** Partial current densities of NH_2OH normalized by electrochemical active surface area for commercial Bi_2O_3 and Bi^{3+}-regenerative system.

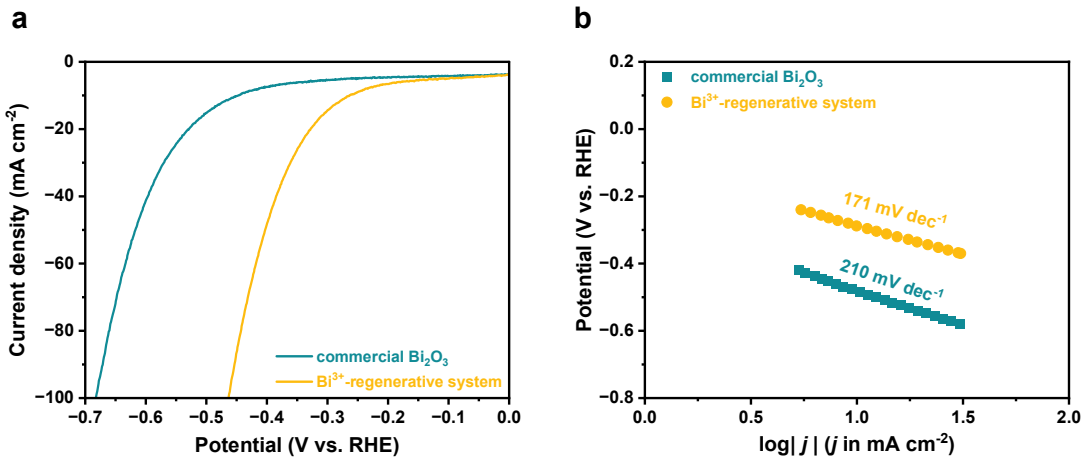

Supplementary Fig. 15 | a, Linear sweep voltammetry (LSV) curves for commercial Bi_2O_3 and Bi^{3+}-regenerative system. **b,** Tafel slopes of electrochemical nitrate reduction over commercial Bi_2O_3 and Bi^{3+}-regenerative system.

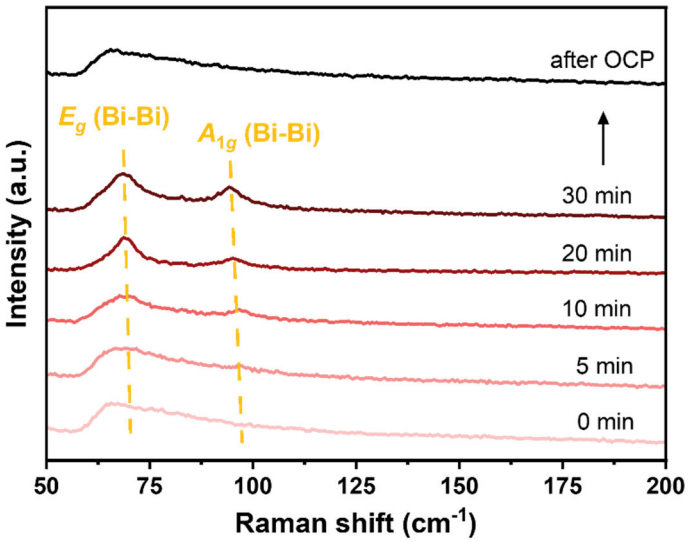

Supplementary Fig. 16 | Operando Raman spectra of metallic Bi signal at the applied potential of -1.4 V vs. RHE.

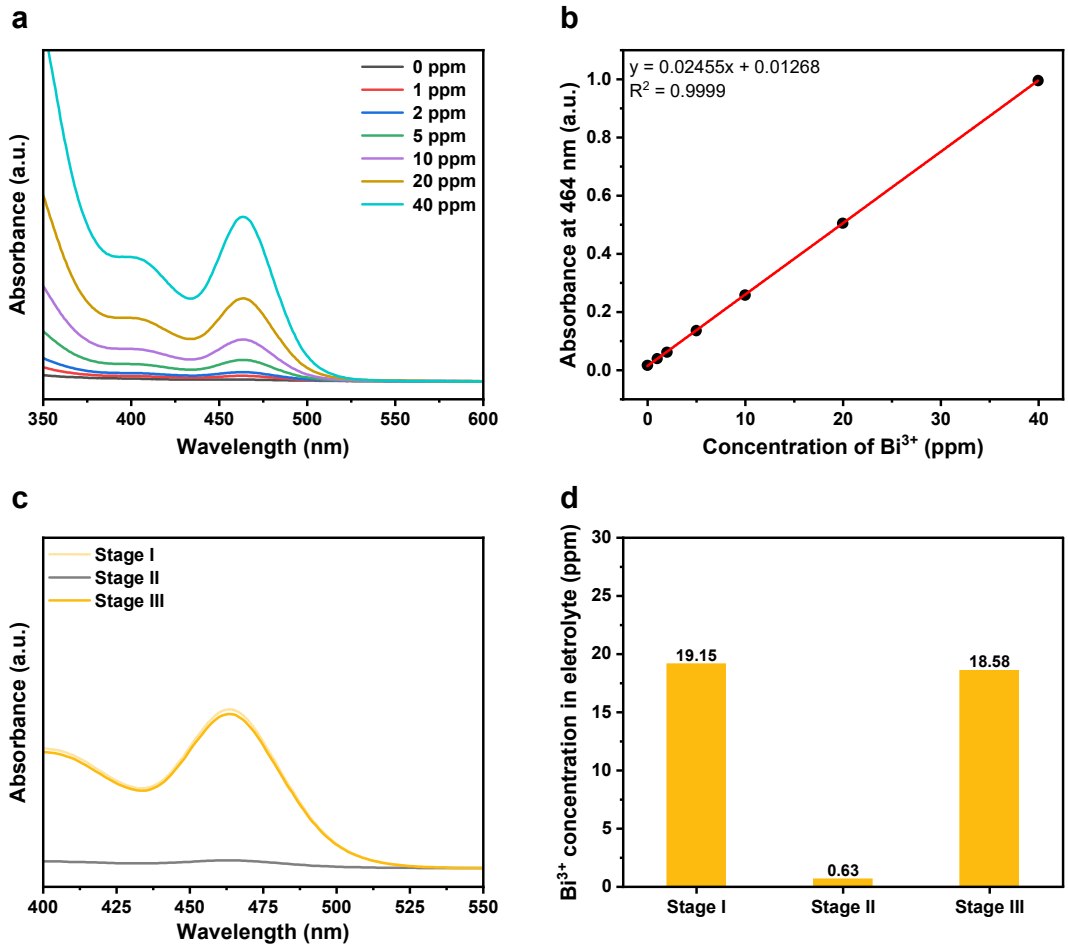

Supplementary Fig. 17 | a, Quantification of Bi^{3+} by colorimetric method. **b,** Calibration curve of Bi^{3+}. **c,** Bi^{3+} absorbance of electrolyte samples in three stages. **d,** Bi^{3+} concentration of electrolyte samples at corresponding stages.

The concentration of Bi^{3+} was quantified using colorimetric methods (Supplementary Fig. 17). Briefly, 0.2 mL of ascorbic acid solution (AA, 10 wt%) and 0.5 mL of potassium iodide solution (KI, 20 wt%) were added to 0.5 ml of the sample solution. After mixing thoroughly and a 5-min reaction period, the absorbance at 464 nm was recorded using an Agilent Cary60 UV-Vis spectrophotometer. A linear calibration curve was established using a series of Bi^{3+} standard solutions ranging from 0 to 40 ppm. To validate the Bi^{3+}/Bi dynamic redox cycle, the Bi^{3+} concentration in electrolyte was monitored across the 3 stages proposed in Fig. 3i. Stage I: the initial electrolyte prior to NO_3^- reduction; Stage II: the post-electrolyte after the NO_3^- reduction; Stage III: the Bi-deposited electrode subjected to open-circuit potential step in fresh Bi^{3+}-free electrolyte.

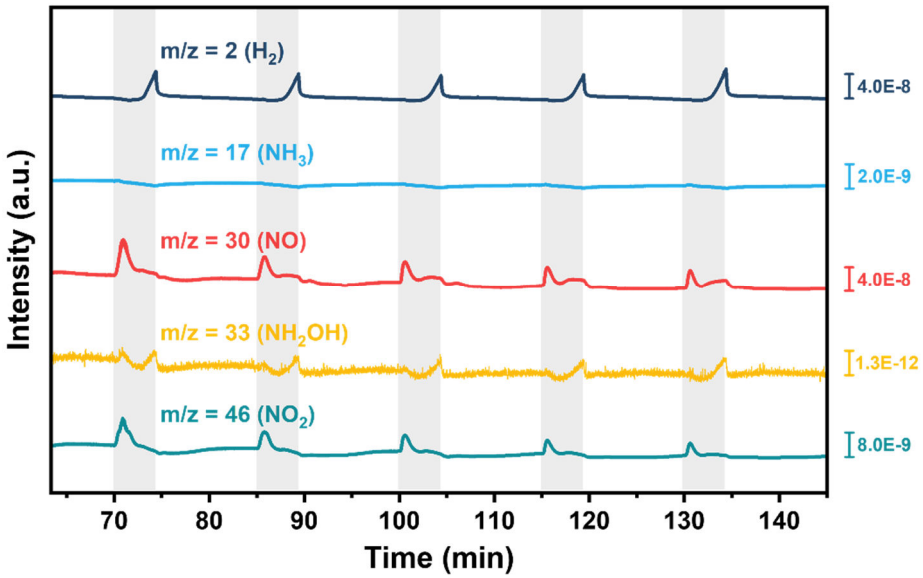

Supplementary Fig. 18 | Online DEMS measurements of electrochemical NO_3^- reduction over five consecutive LSV scans. The grey shaded regions represent the entire LSV scanning process from -0.2 to -1.5 V vs. RHE.

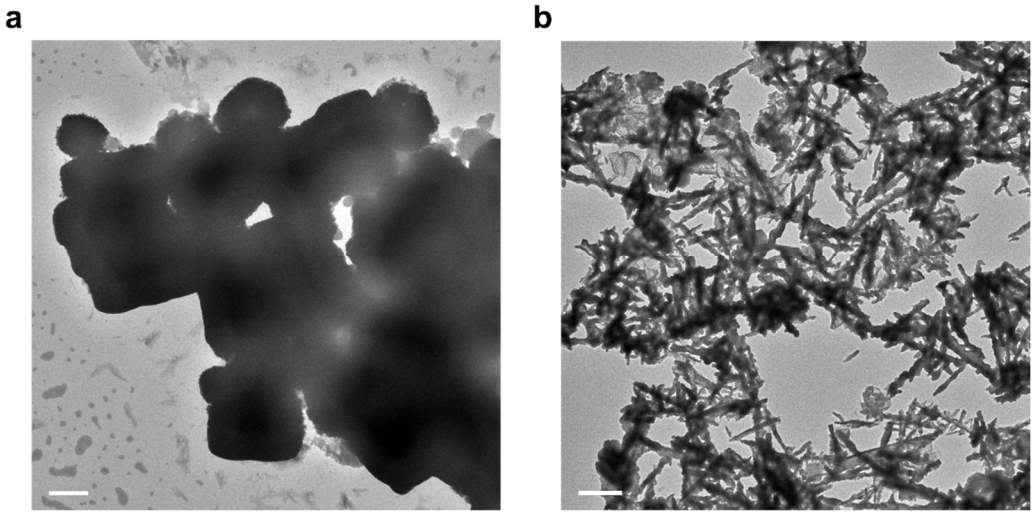

Supplementary Fig. 19 | TEM images after long-term electrolysis under **(a)** continuous and **(b)** intermittent mode. Scale bar: 500 nm.

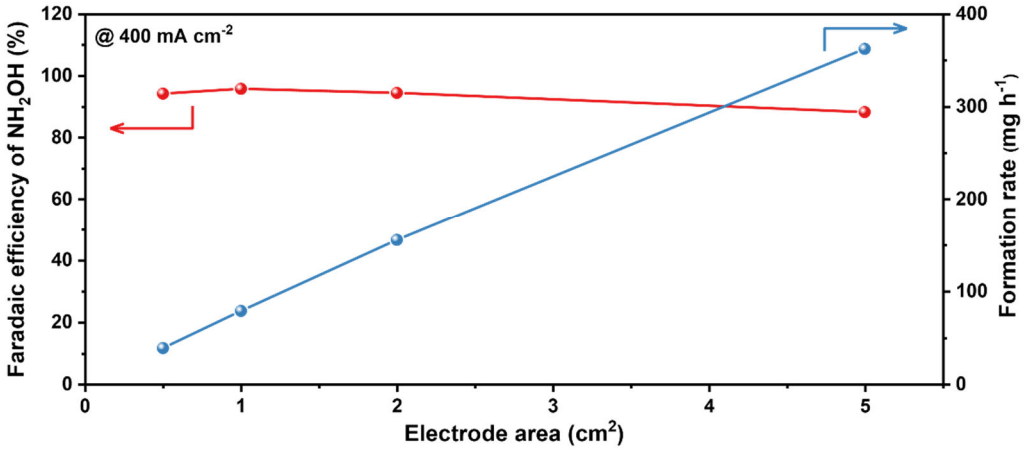

Supplementary Fig. 20 | Faradaic efficiency and formation rate of NH_2OH as a function of the carbon electrode area at a constant current density of 400 mA cm^{-2}.

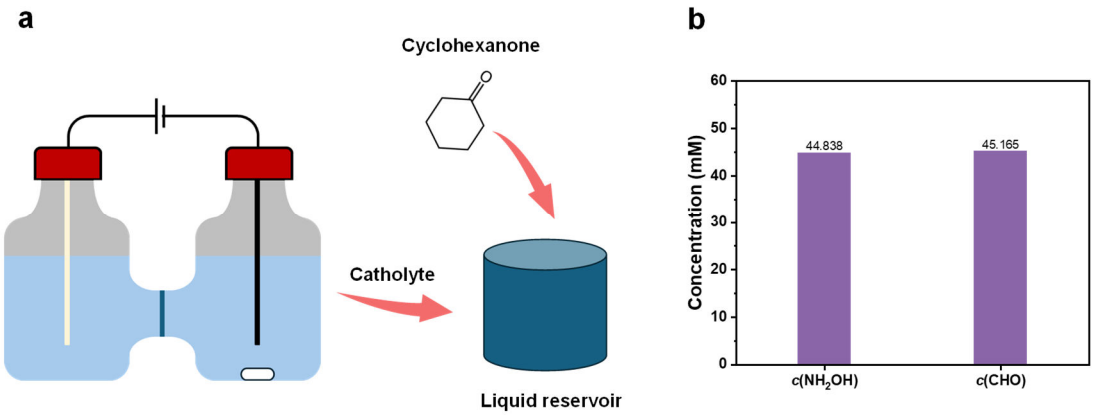

Supplementary Fig. 21 | a, Schematic illustration showing the production of cyclohexanone oxime (CHO) between the upstream catholyte and the introduction of cyclohexanone (CYC). **b,** The concentration of NH_2OH in post-reaction catholyte and the concentration of CHO after the mixture of catholyte and CYC.

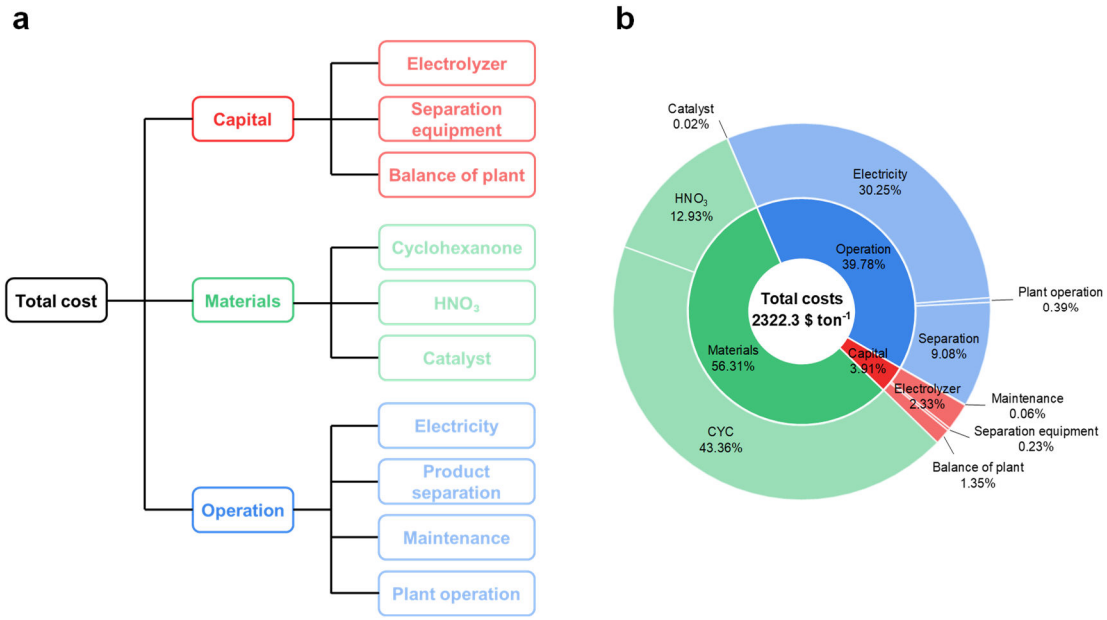

Supplementary Fig. 22 | a, TEA model for the production of cyclohexanone oxime. **b,** Total costs and their components to produce one tonne of cyclohexane oxime per day.

A techno-economic analysis (TEA) with slight modification[5,6] is used to assess the commercial viability of NH_2OH production in our system (Supplementary Fig. 22). NH_2OH is primarily used to react with cyclohexanone to generate cyclohexanone oxime (CHO), which is converted into caprolactam on a large scale for Nylon-6 production in the polymer industry. Therefore, CHO is set as the target derivative in this TEA. The TEA is conducted assuming a daily CHO output of 1 ton (1,000 kg), with the primary variables and calculated metrics summarized as follows:

1. In this model, we assume a cell operation of 0.4 A cm^{-2} with a NH_2OH Faradaic efficiency of 90%.

2. The plant lifetime of 10 years is assumed for the economic evaluation. In a year, the electrolyzers operate for 20 hours daily, utilizing an 83.3% capacity factor to allow for electrolyte replenishment and catalyst regeneration.

3. The electrolyzer cost is assumed to be 10,000 $\$/m^2$.

4. For the input material, we account for the cost from the feedstocks (CYC and HNO_3) and the catalyst ($Bi(NO_3)_3{\cdot}5H_2O$).

5. The separation equipment cost is set as 10% of the electrolyzer cost.

6. The Balance of Plant cost is set as 58% of the electrolyzer cost.

7. The price of electricity is assumed to be 0.1 $/kWh.

8. The product separation cost is considered as 30% of the electricity cost.

9. The maintenance cost is set as 2.5% of the electrolyzer cost.

10. The plant operation cost is assumed to be 10% of the capital costs.

11. The operating voltage is calculated by the following equation:

$$Voltage = E_{OX}^{0} - E_{RE} + E_1 + E_2 + E_3$$

where E_{OX}^{0} is the water oxide potential (1.23 V), E_{RE} is the cathodic potential (-1.23 V), E_1 is the overpotential for water oxidation (0.86 V), and E_2 is the overpotential accounting for the impact of the membrane (1.0 V), and E_3 is the voltage occupied by the solution resistance (0.13 V). Thus, the voltage used in the TEA is determined to be 4.45 V.

To produce 1 ton (1,000 kg) of CHO daily, 867.3 kg of CYC and 291.9 kg of NH_2OH are needed as the feedstocks. The total current is thereby calculated based on the FE of NH_2OH electrosynthesis.

$$Total\ current = \frac{291.9\ kg/day}{20 \times 3600\ s/day} \times \frac{1000\ mol/kmol}{33.03\ kg/kmol} \times \frac{6e^- \times\ 96485\ C/mol}{90\%}$$

$$= 78952\ A$$

The required electrolyzer area is calculated based on total current and estimated current density:

$$Total\ electrolyzer\ area = \frac{78952\ A}{0.4\ A/cm^2} \times \frac{m^2}{10^4\ cm^2} = 19.738\ m^2$$

The power is given from the product of cell voltage and total current:

$$Power = 4.45\ V \times 78952\ A \times \frac{kW}{10^3\ W} = 351.3\ kW$$

Capital Costs:

a) Electrolyzer cost:

The electrolyzer cost can be calculated by the expected price of 10,000 $/m^2:

$$Electrolyzer\ cost = 19.738\ m^2 \times 10000\ \$/m^2 = 197380\ \$$$

b) Separation equipment cost:

The separations equipment associated with the gas/liquid cost in capital costs is assumed to be 10% of the electrolyzer cost:

$$Separation\ equipment\ cost = 197380\ \$ \times 10\% = 19738\ \$$$

c) Balance of Plant cost:

$$Balance\ of\ Plant\ cost = 197380\ \$ \times 58\% = 114480.4\ \$$$

Therefore, the overall capital cost component is calculated as follow:

$$Capital\ costs_{per\ day} = \frac{Electrolyzer\ cost + Separation\ equipment\ cost + Balance\ of\ Plant\ cost}{Plant\ lifetime \times CHO\ production} = \frac{197380\ \$ + 19738\ \$ + 114480.4\ \$}{10\ years \times 365\ day/year \times 1\ ton/day} = 90.8\ \$$$

Materials Costs:

In terms of feedstocks, HNO_3 (68 wt%) and CYC are assumed as 330 $ per ton and 1161 $ per ton, respectively.

$$Feedstock\ cost_{per\ day} = Cost\ of\ HNO_3 \times Mass\ of\ HNO_3 + Cost\ of\ CYC \times Mass\ of\ CYC = \frac{330\ \$/ton}{1000\ kg/ton} \times \frac{1000\ kg \times 63.01\ kg/kmol}{113.16\ kg/kmol \times 90\% \times 68\%} + \frac{1161\ \$/ton}{1000\ kg/ton} \times 867.3\ kg = 300.2\ \$ + 1007\ \$ = 1307.2\ \$$$

The catalyst loading of Bi is 0.6 mg/cm^2. The total catalyst precursor of $Bi(NO_3)_3{\cdot}5H_2O$ is calculated as follow:

$$Mass\ of\ precursor_{per\ time} = 19.738\ m^2 \times \frac{6\ g/m^2}{1000\ g/kg} \times \frac{485.07\ kg/kmol}{208.98\ kg/kmol} = 0.275\ kg$$

The market price of $Bi(NO_3)_3{\cdot}5H_2O$ is conservatively estimated at 50 $ per kilogram. Based on our experimental stability results, a catalyst replacement cycle of 30 days is assumed in the OpEx part to ensure sustained peak performance.

$$Catalyst\ cost_{per\ day} = \frac{50\ \$/kg \times 0.275\ kg}{30} = 0.46\ \$$$

The total material input cost required per day for one ton of CHO production can be calculated below:

$$Material\ cost_{per\ day} = 1307.2\ \$ + 0.46\ \$ = 1307.66\ \$$$

Operation Costs:

a) Electricity cost:

$$Electricity\ cost_{per\ day} = 351.3\ kW \times 20\ hour \times 0.1\ \$/kWh = 702.6\ \$$$

b) Product separation cost:

$$CHO\ separation\ cost_{per\ day} = 702.6\ \$ \times 30\% = 210.78\ \$$$

c) Maintenance cost:

$$Maintenance\ cost_{per\ day} = \frac{197380\ \$ \times 2.5\%}{10\ year \times 365\ day/year \times 1\ ton/day} = 1.35\ \$$$

d) Plant operation cost:

$$Plant\ operation\ cost_{per\ day} = 90.8\ \$ \times 10\% = 9.08\ \$$$

Therefore, the overall operation costs are calculated as follows:

$$Operation\ costs_{per\ day} = 702.6\ \$ + 210.78\ \$ + 1.35\ \$ + 9.08\ \$ = 923.81\ \$$$

Thus, the total cost to electro-synthesize 1 ton of CHO per day is presented:

$$Total\ cost_{per\ day}$$
$$= Capital\ costs_{per\ day} + Materials\ costs_{per\ day}$$
$$+ Operation\ costs_{per\ day} = 90.8\ \$ + 1307.66\ \$ + 923.81\ \$ = 2322.27\ \$$$

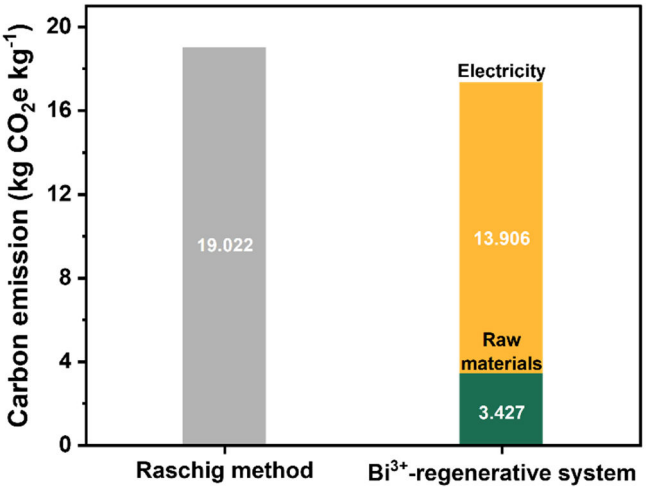

Supplementary Fig. 23 | Carbon emissions for the production of 1 kg of NH_2OH via Raschig method and Bi^{3+}-regenerative system.

This life-cycle assessment study adopts a cradle-to-gate boundary to evaluate the environmental impact of NH_2OH production, comparing industrial route with our proposed electrochemical process (Supplementary Fig. 23). In terms of conventional NH_2OH synthesis, the Raschig method is used, where the feedstocks of ammonia, air, and sulfur dioxide undergo a cascade reaction sequence, giving a total carbon emission factor of 19.022 kg CO_2e per kg of NH_2OH (obtained from Ecoinvent 3.10 database). In our electrochemical process, we assume that carbon footprint consists of three primary contributions: raw materials, electrolysis process, and downstream management.

Inventory of electrochemical NH_2OH synthesis

a) CO_2 emissions from raw materials: In the proposed electrocatalytic process, HNO_3 is identified as the primary feedstock that contributes to upstream carbon footprint. The corresponding carbon factor is listed in Supplementary Table 2 (obtained from Ecoinvent 3.10 database). Due to ultra-low loading and high sustainability of the bismuth nitrate catalyst, its environmental impact is assumed negligible relative to the consumption of HNO_3 and is thus excluded from the inventory.

Therefore, to produce one kilogram of NH_2OH, its carbon emissions can be calculated below:

$$GWP_{raw\ materials} = \frac{63.01\ kg/kmol}{33.03\ kg/kmol} \times 1\ kg \times 1.7962\ kg\ CO_2e/kg = 3.427\ kg\ CO_2e$$

b) CO_2 emissions during electrolysis: The carbon footprint of electrochemical process is dominated by the operation of the electrolyzer. To provide a comprehensive assessment, two distinct energy sources are considered[7]: national grid electricity (representing current industrial conditions) and renewable electricity (representing green and low-carbon expectations). The CO_2 emissions related to fabrication of electrolyzer and auxiliary separation hardware are omitted. This is supported by previous findings that carbon footprint for infrastructure is typically several orders of magnitude lower than that of materials and operation[8]. The carbon emissions in this part are calculated based on the electricity consumption for 1 kg of NH_2OH generation and the relative carbon factor. The cell voltage and Faradaic efficiency are assumed as 4.45 V and 90%, respectively.

$$Electricity\ consumption = \frac{1000\ g \times 6e^- \times 96485\ C/mol \times 4.45\ V}{33.03\ g\ /mol \times 90\%} \times \frac{1\ kWh}{3.6 \times 10^6\ J}$$

$$= 24.072\ kWh$$

Therefore, the carbon emissions for electrolysis process are calculated as follows, where $EF_{electricity}$ is the carbon factor of electricity in Supplementary Table 1.

$$GWP_{electrolysis} = Electricity\ consumption \times EF_{electricity}$$

$$= 24.072\ kWh \times 0.5777\ kg\ CO_2e/kWh = 13.906\ kg\ CO_2e$$

c) CO_2 emissions for downstream management: The downstream application of NH_2OH is predominantly centered on the oximation with ketone or aldehyde, which accounts for approximately 95% of its total industrial production (e.g. the synthesis of cyclohexanone oxime). In our electrocatalytic system, the high FE of NH_2OH, combined with precise potential control of Bi deposition and stripping, ensures a high-purity and metal salt-free NH_2OH solution. The as-prepared electrolyte can be thus directly coupled with cyclohexanone, achieving ~100% yield of cyclohexanone oxime (as confirmed in Supplementary Figure 22). In this scenario, the energy-intensive process of isolating free NH_2OH is circumvented, allowing the focus to shift towards highly efficient oxime separation (e.g. via liquid-liquid extraction). Therefore, within the "gate-to-gate" scope of NH_2OH synthesis, the carbon footprint is considered negligible when comparing above two routes because NH_2OH produced

via Raschig method serves the same downstream oximation purpose.

Supplementary Table 1 | Comparison of FE and productivity for electrosynthesis of NH_2OH in our work and reported literature.

Catalyst	N source	Electrolyte	FE (%)	Productivity (mmol h^{-1} cm^{-2})	Ref.
Bi^{3+}/Bi redox cycle	NO_3^-	HNO_3 (0.5 M)	91.0	2.912	This work
		HNO_3 (1 M)	86.5	4.568	
Bi/CFP	NO_3^-	$HNO_3 + H_2SO_4$	81	0.713	[3]
Bi NSs	NO_3^-	$HNO_3 + KNO_3$	86.6	2.03	[9]
Au	NO_3^-	HNO_3	34.2	0.2301	[10]
ZnPc	NO_3^-	$KNO_3 + KOH$	53	2.52	[11]
FePc/KB	NO_2^-	$KNO_2 + KHCO_3$	52.6	2.45	[12]
			50.5	2.35	[12]
Co SACs	NO	PBS (pH 7)	81.3	0.163	[13]
SA-Fe	NO	$K_2SO_4 + H_2SO_4$	74.3	0.93	[14]
Cu-MnO_2H_x	NO_3^-	$KNO_3 + K_2SO_4$ + acetone	91.1	0.3966	[15]
TiO_2	NO_3^-	KNO_3 + KOH + HCHO	92.6	2.085	[16]
Zn-Cu	NO_3^-	KNO_3 + KPi + CYC	27	0.168	[17]
R-TiO_2	NO_3^-	$KNO_3 + NaCO_3/NaHCO_3$ + CYC	68.2	0.1273	[18]
A-Mn	NO_3^-	KNO_3 + KOH + HCHO	40.92	0.251	[19]
$Cu_xC_yO_z$@600	NO_3^-	KNO_3 + cyclopentanone	47.8	0.352	[20]
PdCuAgBiln	NO_2^-	KNO_2 + PBS + CYC	47.6	0.288	[21]
Ag	NO_2^-	$NaNO_2 + Na_2CO_3$ + CYC	83.8	0.78	[22]

Supplementary Table 2 | Equivalent carbon emission constants in LCA.

Items	Values	Unit
NH_2OH	19.0224	kg CO_2e kg^{-1}
HNO_3	1.7962	kg CO_2e kg^{-1}
Grid (China)	0.5777	kg CO_2e kWh^{-1}
Renewable electricity (photovoltaic)	0.0520	kg CO_2e kWh^{-1}
Renewable electricity (wind)	0.0324	kg CO_2e kWh^{-1}

References:

1. Tamtaji, M. *et al.* A high-entropy single-atom catalyst toward oxygen reduction reaction in acidic and alkaline conditions. *Adv. Sci.* **11**, 2309883 (2024).
2. Pang, Y. *et al.* Porous Bi nanosheets derived from β-Bi_2O_3 for efficient electrocatalytic CO_2 reduction to formate. *ACS Appl. Mater. Interfaces* **16**, 42109-42117 (2024).
3. Kong, X. *et al.* Synthesis of hydroxylamine from air and water via a plasma-electrochemical cascade pathway. *Nat. Sustain.* **7**, 652-660 (2024).
4. Zhou, X., Tamtaji, M., Zhou, W., Goddard, W. A., III & Chen, G. Nonprecious triple-atom catalysts with ultrahigh activity for electrochemical reduction of nitrate to ammonia: A DFT screening. *ACS Appl. Mater. Interfaces* **17**, 4854-4864 (2025).
5. Yuan, Y. *et al.* Electrocatalytic ORR–coupled ammoximation for efficient oxime synthesis. *Sci. Adv.* **10**, eado1755
6. Li, J. *et al.* Managing electrolyte flow boosts the efficiency of continuous oxime electrosynthesis to over 95%. *Nat. Commun.* **17**, 1970 (2026).
7. Announcement on the release of 2024 electricity carbon footprint factor data, https://www.mee.gov.cn/xxgk2018/xxgk/xxgk01/202510/t20251024_1130734.html (2025).
8. De Luna, P. *et al.* What would it take for renewably powered electrosynthesis to displace petrochemical processes? *Science* **364**, eaav3506 (2019).
9. Ni, J. *et al.* Revealing the role of interfacial water in pH-dependent hydroxylamine electrosynthesis over Bi-based catalysts. *ACS Catal.* **15**, 15153-15161 (2025).
10. Xie, Y. *et al.* Electrochemical reduction of nitrate to hydroxylamine on gold electrode. *Chem. Commun.* **60**, 10918-10921 (2024).
11. Tang, Y. *et al.* Selective electrosynthesis of hydroxylamine from aqueous nitrate/nitrite by suppressing further reduction. *Nat. Commun.* **15**, 9800 (2024).
12. Li, J. *et al.* Sustainable oxime production via the electrosynthesis of hydroxylamine in a free state. *Nat. Synth.* **4**, 1598-1609 (2025).
13. Zhou, J. *et al.* Linear adsorption enables no selective electroreduction to hydroxylamine on single Co sites. *Angew. Chem. Int. Ed.* **62**, e202305184 (2023).
14. Zhao, S. *et al.* Selective nitric oxide electroreduction at monodispersed transition-metal sites with atomically precise coordination environment. *Chem Catal.* **3**, 100598 (2023).
15. Guo, C., Guo, M., Zhang, Y., Han, S. & Yu, Y. Lattice hydrogen involved electrocatalytic nitrate reduction to hydroxylamine. *J. Am. Chem. Soc.* **147**, 14869-14877 (2025).
16. Zhang, J. *et al.* Electrochromic rutile with dynamically tailored surfaces in formaldehyde-mediated hydroxylamine electrosynthesis. *J. Am. Chem. Soc.* **147**, 20559-20570 (2025).
17. Sharp, J. *et al.* Sustainable electrosynthesis of cyclohexanone oxime through nitrate reduction on a Zn–Cu alloy catalyst. *ACS Catal.* **14**, 3287-3297 (2024).
18. Luo, L. *et al.* Electrosynthesis of the nylon-6 precursor from nitrate and cyclohexanone over a rutile TiO_2 catalyst. *CCS Chem.* **7**, 266-278 (2024).
19. Lan, X. *et al.* Electrosynthesis of hydroxylamine from nitrate reduction in water. *Sci. China Chem.* **66**, 1758-1762 (2023).
20. Jia, S. *et al.* Synthesis of hydroxylamine via ketone-mediated nitrate electroreduction. *J. Am. Chem. Soc.* **146**, 10934-10942 (2024).
21. Sheng, Y. *et al.* Modulating hydrogen adsorption by unconventional p–d orbital hybridization over porous high-entropy alloy metallene for efficient electrosynthesis of nylon-6 precursor.

Angew. Chem. Int. Ed. **63**, e202410442 (2024).

22. Zhang, F. *et al.* A Pickering-emulsion-droplet-integrated electrode for the continuous-flow electrosynthesis of oximes. *Nat. Synth.* **4**, 479-487 (2025).